Iron-based fluorophosphate Na_2FePO_4F as a cathode for aqueous zinc-ion batteries†

Deepa Singh, [a] Yang Hu, [b] Sher Singh Meena, [c] Rishikesh Vengarathody, [b] Maximilian Fichtner [bd] and Prabeer Barpanda *[abd]

Aqueous zinc-ion batteries form a key post-Li-ion batteries to cater the rising demand for grid storage. Fe-based compounds can be used as economical cathodes for zinc-ion batteries. Herein, we explored iron-based flourophosphate as a potential polyanionic cathode. Involving the $Fe^{3+/2+}$ redox process, it can reversibly intercalate Zn^{2+} yielding a capacity of ~80 mA h g^{-1}, involving a solid-solution mechanism. Polyanionic Fe-based phosphate frameworks can be harnessed as potential low-cost cathodes for secondary zinc-ion batteries.

The rising demand for energy in the present century presents a daunting challenge to find suitable alternatives to Li-ion battery technology to fulfil the demand of grid storage.[1–3] Although Li-ion batteries remain unchallenged in the portable electronics sector, their mass-scale deployment in stationary storage can be expensive.[4] The scarcity of raw materials,[5] meticulous manufacturing constraints, and using hazardous and flammable non-aqueous electrolytes limit the possibility of scaling up lithium-based energy storage systems.[6] In this scenario, various post-Li-ion batteries, including multivalent batteries are vying for wide scientific attention. Due to elemental abundance, the availability of economic raw materials, and environmentally benign and safe electrolytes, zinc-ion batteries have emerged as promising post-Li-ion batteries.[7,8] However, there are issues, such as dendrite formation at the Zn anode.[9] Various classes of aqueous cathodes have been explored for zinc-ion batteries (ZIBs), such as manganese-based oxides,[10–14] vanadium-based oxides,[15,16] Prussian blue analogues,[17] and phosphates.[18] While the intercalation-based mechanism is widely examined for high reversibility, there are recent reports on redox activity based on conversion[19] or co-insertion of H^+ and Zn^{2+}.[20] On a similar note, polyanionic host materials having three-dimensional open framework structures have been investigated for aqueous rechargeable batteries.[18] Recently, NASICON structures have been used as zinc-ion battery cathodes due to their open framework and thermodynamic stability. In particular, $Na_3V_2(PO_4)_3$ was studied in 1 M $Zn(NO_3)_2$, providing a discharge capacity of over 50 mA h g^{-1} with 93% capacity retention after ten cycles.[21] Furthermore, Li *et al.*[22] reported graphene-like carbon-wrapped $Na_3V_2(PO_4)_3$ as a cathode for aqueous ZIBs in 0.5 M $Zn(CH_3COO)_2$ electrolyte, which delivered a reversible capacity of 97 mA h g^{-1} at 0.5C and retained 74% capacity. The introduction of fluorine is known to enhance the potential of the cathode owing to its inductive effect. In that pursuit, a fluorophosphate $Na_3V_2(PO_4)_2F_3$ cathode was reported as a 1.62 V cathode with an energy density of 98 W h kg^{-1} using a carbon-coated Zn metal anode.[23] Manthiram's group[24] carried out the detailed mechanistic studies on $Zn/Na_3V_2(PO_4)_2F_3$ material in both non-aqueous and aqueous media. Additionally, Wang *et al.*[25] reported a high energy (218 W h kg^{-1}) and power density (8000 W kg^{-1}) cathode for aqueous ZIBs with 4 M zinc trifluoromethanesulfonate ($Zn(Otf)_2$) as an electrolyte. Recently, Ni *et al.*[26] employed a neutral water-in-bisalt-based electrolyte comprising 25 M $ZnCl_2$ + 5 M NH_4Cl and reported an rGO-wrapped $Na_3V_2(PO_4)_2O_{1.6}F_{1.4}$ as a potential cathode. Pursuing phosphate chemistry, Manthiram's group reported a favorite-based VPO_4F as a cathode for both aqueous and non-aqueous ZIBs.

While most of these ZIB cathodes are based on vanadium chemistry, they suffer from toxicity and difficulty in large-scale dissemination. In contrast, Fe-based compositions can provide economic and eco-friendly cathode candidates. Exploring Fe-based polyanionic frameworks, herein, we investigated earth-abundant iron-based fluorophosphate $Na_2Fe^{II}PO_4F$ (NFPF) as a potential cathode for ZIBs. NFPF was synthesized using solution combustion synthesis involving low-cost Fe^{III} precursor. The details of the material synthesis are elaborated in ESI.† Rietveld analysis of the resulting product was carried out using the FullProf suite.[27] Reliable refinement parameters (a Bragg *R*-factor of 8.561, R_F of 7.834, and χ^2 of 9.59) were obtained with the framework assuming an

[a] *Faraday Materials Laboratory (FaMaL), Materials Research Centre, Indian Institute of Science, Bangalore 560012, India. E-mail: prabeer@iisc.ac.in*
[b] *Helmholtz Institute Ulm (HIU), Electrochemical Energy Storage, Ulm 89081, Germany*
[c] *Solid State Physics Division, Bhabha Atomic Research Centre, Mumbai, 400085, India*
[d] *Institute of Nanotechnology, Karlsruhe Institute of Technology (KIT), Karlsruhe 76021, Germany*

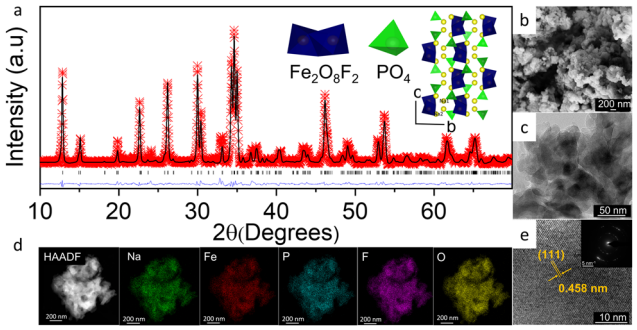

Fig. 1 (a) Rietveld refined powder X-ray diffraction (XRD) pattern of Na_2FePO_4F synthesized at 600 °C for 6 h in Ar atmosphere (source: Cu $K_{\alpha 1}$, λ = 1.5406 Å). The experimental data points (red stars), calculated diffraction pattern (black line), their difference (blue line), and the Bragg positions (black ticks) are shown. Inset (left) $Fe_2O_8F_2$ dioctahedra (blue) and PO_4 tetrahedra (green) units. (right) Crystal structure of Na_2FePO_4F assuming orthorhombic structure having $Fe_2O_8F_2$ (blue) abridged with PO_4 units (green). (b) SEM of Na_2FePO_4F shows agglomerated and porous morphology. (c) Transmission electron micrograph of Na_2FePO_4F. (d) Elemental distribution maps showing homogeneous distribution of Na (green), Fe (red), P (blue), F (pink), and O (yellow). (e) HRTEM and SAED pattern (inset) confirming the crystalline nature, where the *d* spacing of 0.458 nm belongs to (111) crystallographic plane.

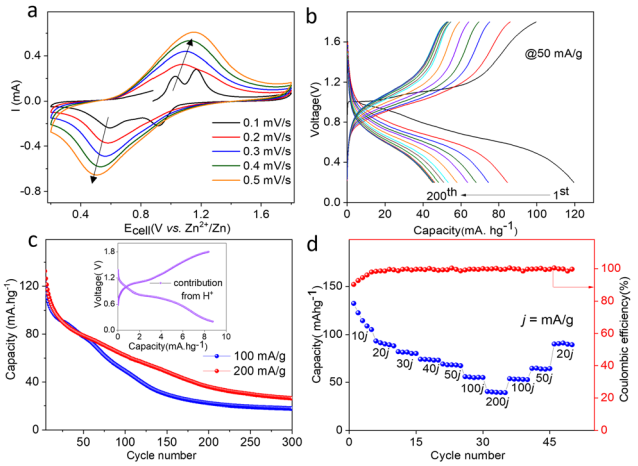

Fig. 2 Electrochemical performance of Na_2FePO_4F. (a) Cyclic voltammogram of Na_2FePO_4F cell in 3M Zn $(Otf)_2$ at five different scan rates. (b) Galvanostatic cycling for 200 cycles (at 50 mA g^{-1}). (c) Cycling stability of Na_2FePO_4F at two different current rates (100 mA g^{-1} and 200 mA g^{-1}) with small proton contribution towards the capacity (inset). It shows drastic fading after 200 cycles. (d) Rate kinetics of Na_2FePO_4F at different current rates.

orthorhombic structure (*e.g. Pbcn*), as shown in Fig. 1a. The final lattice parameters were: a = 5.2065(17) Å, b = 13.8197(5) Å, c = 11.7553(4) Å, and vol = 845.82(1) $Å^3$. Additional refinement details are provided in Table S1 (ESI†). NFPF has a layered structure consisting of $[FeO_4F_2]$ octahedra and $[FeO_8F_2]$ bi-octahedra that are connected *via* F atoms giving rise to two distinct crystallographic sites of the constituent sodium species (Fig. 1a, inset). A small amount of maricite $NaFePO_4$ impurity peak was detected at $2\theta \sim 24°$.

Solution combustion synthesis generally leads to agglomerated and porous morphology. Here, the morphology of the NFPF product was analysed using scanning and transmission electron microscopy (SEM and TEM). SEM micrographs showed agglomerated morphology with the sub-micro particle range (Fig. 1b). TEM revealed that these primary particles consisted of secondary particles in the size range of 100–200 nm (Fig. 1c). EDS analysis showed a uniform distribution of all the elements. The quantification is shown in Fig. S1 and Table S2 (ESI†). HRTEM showed a *d* spacing of 4.58 Å corresponding to the *hkl* plane of (111) (Fig. 1d). The SAED pattern confirmed the high crystallinity of NFPF.

Furthermore, the NFPF powder was used to prepare the slurry of the working electrode by mixing it with Super P carbon black and PVDF binder (70:20:10) in *N*-methyl-2-pyrrolidone (NMP) and was coated on a stainless-steel current collector. After drying the electrodes in a vacuum oven, they were used to assemble half cells with a mass loading of 4–5 mg cm^{-2} (ESI†). Cyclic voltammetry was carried out in 3 M $Zn(Otf)_2$, showing two cathodic peaks at 1.02 V and 1.17 V, and the two anodic peaks at 0.58 V and 0.924 V, showing the consecutive insertion/deinsertion of Zn^{2+} in first cycle. In the subsequent cycles, they merged to form a single peak which may be due to irreversible structural arrangement during the 1st cycle (Fig. 2a). The galvanostatic studies for Zn-ion intercalation were conducted in the voltage window of 0.2–1.8 V. First, the Zn-ion cell was charged up to 1.8 V to remove sodium and then discharged to 0.2 V to intercalate Zn in the system. During the first discharge, Zn-ions start replacing Na-ions *via* progressive insertion in the desodiated host structure, providing the initial discharge capacity of 124 mA h g^{-1}. The voltage profile shows a significant difference in consecutive cycles. The capacity degradation was observed even at lower current rates of 50 mA g^{-1}, suggesting that Zn insertion kinetics is sluggish (Fig. 2b). Similar behaviour was observed at higher currents of 100 mA g^{-1} and 200 mA g^{-1}, where the capacity degraded drastically after 100 cycles (Fig. 2c). During the cycling, proton (de)insertion had a negligible contribution, with most capacity arising from Zn^{2+} (de)insertion. A meager (8 mA h g^{-1}) proton contribution was found in 10 mM H_2SO_4 electrolyte (Fig. 2c, inset), which can lead to variation in pH and the formation of byproducts. The rate capability showed the retention of the structure at 200 mA g^{-1} (Fig. 2d). Further, when the galvanostatic cycling was carried out in the 2 M $Zn(TFSI)_2$ electrolyte, it still showed huge degradation in the capacity (Fig. S2, ESI†). Overall, the rate kinetics was found to be sluggish due to the rigid three-dimensional framework and the structural instability of fluorophosphate at higher currents for feasible Zn (de)insertion.

To understand the structural shortcomings of ZIBs, a series of studies were carried out at different depths of discharge (DOD) and states of charge (SOC). A comparative ^{57}Fe Mössbauer spectra (MS) of the NFPF cathodes (at room temperature) are depicted in Fig. 3a and their parameters are tabulated in Table S3 (ESI†). The majority of Fe^{2+} (high spin) species were recorded in the pristine material. The doublets, red and green, represented Fe^{2+} and Fe^{3+}, respectively. Upon charging and discharging, the expected Fe^{2+}/Fe^{3+} redox process was captured. The difference in oxidation state was further proved by *ex situ* XANES analysis, which was fitted using the Athena program (Fig. 3b). It is observed that the K-edge of standard FeO and pristine NFPF at an open-circuit voltage (OCV) and DOD 0.2 V showed a similar edge energy position corresponding to the

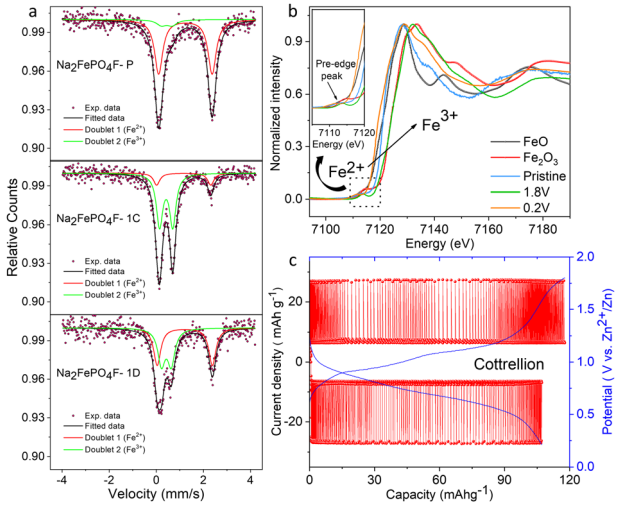

Fig. 3 (a) *Ex situ* Mössbauer spectra of Na_2FePO_4F cathode at three states (pristine, 1st charge, and 1st discharge) revealing the change in oxidation states for the Fe^{2+}/Fe^{3+} redox centre. (b) Corresponding XANES spectra of $Na_{2-x}FePO_4F$ cathodes. (c) Cottrell type potentiometric titration curve confirming underlying solid-solution mechanism.

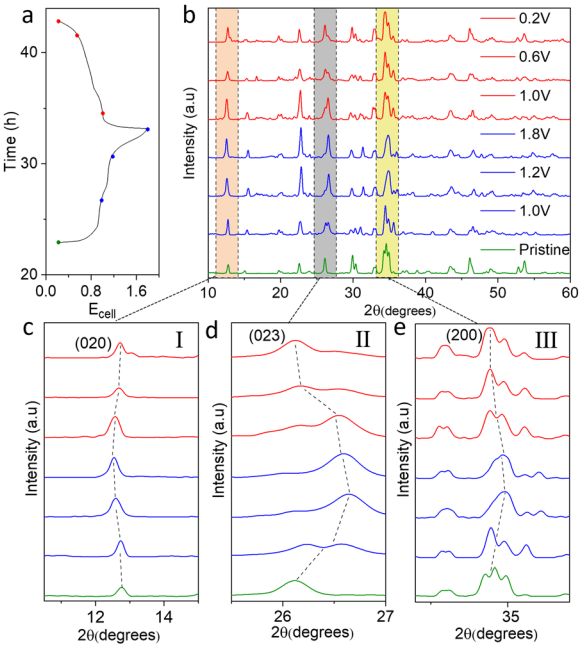

Fig. 4 (a) and (b) *Ex situ* XRD patterns of Na_2FePO_4F cathode at different DOD and SOC during the 1st cycle displaying the changes along planes with *hkl* values of (020), (023), and (200) represented as (c) I, (d) II, and (e) III.

Fe^{2+} state. After the 1st charge, the Fe K-edge shifted to a higher energy close to the Fe_2O_3 standard, indicating a formal oxidation state close to Fe^{3+}. There is also a noticeable change in the coordination sphere, which was studied using EXAFS (description in ESI,† Fig. S3). After 1st discharge, the interatomic distances were all shorter than those obtained from the pristine electrode, implying that the local environment of Fe was not fully reverted to the pristine state. NFPF and NFPF-1D showed some similarity, and NFPF-1C exhibited distinct spectra features and notably higher amplitude in $|\chi(R)|$. Furthermore, the PITT study revealed a typical Cottrell-type curve with a constant current response throughout the cycle. It signifies the occurrence of a continuous solid-solution (single phase) redox reaction during cell operation. It revealed the (de)intercalation of Zn^{2+} ions from the pristine cathode structure in the potential window of 0.2 to 1.8 V (Fig. 3c).

To gauge the underlying redox mechanism, *ex situ* X-ray diffraction analysis was carried out for the 1st cycle at different SOC and DOD. The charged states were 1 V, 1.2 V and 1.8 V; discharged states were 1 V, 0.6 V, and 0.2 V respectively. In the pristine state, NFPF peaks at 2θ values of 12.74°, 26.1°, and 34.5° were considered. A gradual peak shift was observed upon Zn^{2+} insertion in the host cathode (Fig. 4), suggesting a solid solution (monophasic) redox mechanism in agreement with the PITT study. A closer look at the *ex situ* XRD patterns revealed a gradual shift in the three distinct peaks highlighted as regions I, II, and III in Fig. 4.

During charging, the (020) at 12.74° shifted to a lower 2θ value of 12.53° due to an expansion along the *b*-axis. Furthermore, the peak at 26.11° shifted to higher 2θ values at 26.60°, indicating a decrease in *d* spacing. Also, this peak shifted with the splitting at SOC of 1.0 V, which further converged into a single peak and then again split into two peaks at DOD of 1.0 V and became a single peak at the end of the discharge matching with the pristine XRD pattern. The peak at 34.61° shifted to a higher 2θ value of 34.87°, where the split peak became a single peak at the end of charge and then again split back at the end of discharge at 0.2 V. This splitting and merging of (023) and (200) peaks may involve other reactions associated with by-product formation, which are reversible in the first cycle and not visible through XRD. Overall, solid solution behaviour is observed at the end of the 1st cycle.

To gauge the reversibility, we extended the *ex situ* XRD studies for higher cycles (1st, 2nd, 5th, and 10th cycles) (Fig. 5). A significant change was observed after the 10th cycle, where most of the reflections of the parent structure were lost. However, there was an important observation at the multiple split peaks in the 2θ range of 32–35°. The peak present at 32.98° got intensified and became a prominent peak at the end of the 10th cycle, meaning the major (de)intercalation is happening along the related (012) plane. The highly intense split (triplet) peak at 34.55° merged and became a doublet and less intense at the end of the 10th cycle. It can arise due to the gradual transformation of the initial phase to a hydrated form of zinc hydroxy triflate, $[Zn_x(Otf)_2(OH)\cdot xH_2O]$ (ZHT) that belongs to the category of LDH (layered doubled hydroxide). This phase change was not spontaneous by simply soaking the electrode in 3 M $Zn(Otf)_2$ electrolyte (Fig. S4a, ESI†). Also, the pristine electrode was found to be thermally stable up to 400 °C (Fig. S4b, ESI†). The ZHT has a signature peak at 2θ value of 33°.[28] ZHT was deposited on the surface, starting from the first cycle. This was confirmed using X-ray diffraction taken at the 10th discharge. To probe it further, *ex situ* SEM and *ex situ* XPS analyses were conducted. The *ex situ* SEM images taken after the 2nd, 5th, and 10th charge, and discharge showed significant differences in morphology (description in ESI,† Fig. S5a–f). In the Zn side, though there are no substantial changes in the peak position in the XRD patterns of cycled Zn anode (Fig. S6a, ESI†), there is still

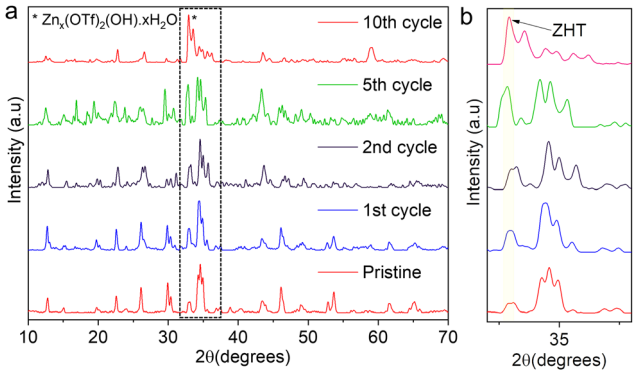

Fig. 5 (a) *Ex situ* XRD patterns of Na_2FePO_4F for ten cycles at complete discharged state showing the highlighted region (dotted black) and changes along that *hkl* plane (b).

an observable intensity change in peaks present at 36.3° and 38.9°. It can arise due to the preferential deposition of Zn after some cycles (Fig. S6b and c: yellow dotted circles, ESI†). Thus, upon longer cycling, the formation of Zn dendrites was also responsible for the degradation of the overall capacity. Similar capacity degradation has been observed in V-based cathode materials.[29]

X-ray photoelectron spectroscopy (XPS) suggested apparent changes in the oxidation state. Full explanation of XPS is provided in ESI† (Fig. S7–S9). In SEM-EDS of the cycled cathode, ZHT was present after the 10th cycle (Fig. S10a–d, ESI†). Also, the results of the cycled Zn XPS were in correlation with SEM-EDS, where there is only deposition of zinc hydroxy fluorinated species over the surface in the form of flakes (Fig. S11a and b, ESI†). FTIR confirmed the presence of –OH on both cathodes and the anode side (Fig. S12a and b, ESI†). Overall, the structural changes during Zn (de)insertion have been schematically presented in Fig. S13 (ESI†). First, pristine $Na_2Fe^{II}PO_4F$ undergoes desodiation after the first charge to 1.8 V forming $NaFe^{III}PO_4F$. In the following discharge to 0.2 V, Zn insertion occurs in the vacant Na site leading to the formation of $Zn_xNa_yFePO_4F$.

In summary, an economic Fe-based fluorophosphate polyanionic framework, Na_2FePO_4F, was reported as a cathode for aqueous zinc-ion batteries. Following the first charge (desodiation), it reversibly uptake Zn^{2+} to deliver a capacity of ~80 mA h g^{-1}. The corresponding Fe^{2+}/Fe^{3+} redox activity was confirmed by Mössbauer and XANES spectroscopy. *Ex situ* XRD study suggested an underlying solid-solution redox mechanism during Zn (de)insertion. During prolonged cycling, an irreversible formation of $Zn_x(OTf)_y(OH)_{2x-y}\cdot xH_2O$ (ZHT) phase at the cathode surface was noticed, which acts as an impediment for further Zn (de)intercalation leading to capacity fading. On the anode side, cycled Zn metal showed an evolution of the surface morphology to nanoflakes, possibly because of the deposition of fluorinated species from the electrolyte. Overall, there is a presence of Zn dissolution-deposition and a co-insertion of H^+/Zn^{2+} along with the deposition of ZHT. The underlying phase transformations and related performance degradation in iron-based fluorophosphates warrant further investigation using various *in situ* techniques. The electrochemical performance of these materials can be improved using electrolyte engineering with additives or high-concentration salts, structural design modifications, and doping strategy.[30] While the capacity and rate kinetics are limited for iron fluorophosphate, this study shows that Fe-based phosphoanionic cathodes can be implemented in aqueous zinc-ion batteries.

We acknowledge the financial support from the Technology Mission Division (Govt. of India) (DST/TMD/MES/2k18/00217). D. S. thanks the MHRD (Govt. of India) for financial support. P. B. is grateful to the Alexander von Humboldt Foundation (Bonn) for a 2022 Humboldt fellowship for experienced researchers. Crystal structures were illustrated using the VESTA software.[31]

Conflicts of interest

The authors declare no conflict of interest.

Notes and references

1 D. Larcher and J. M. Tarascon, *Nat. Chem.*, 2015, **7**, 19–29.
2 M. S. Whittingham, *Proc. IEEE*, 2012, **100**, 1518–1534.
3 T. M. Gurr, *Energy Environ. Sci.*, 2018, **11**, 2696–2767.
4 M. Armand and J. M. Tarascon, *Nature*, 2008, **451**, 652–657.
5 T. C. Wanger, *Conserv. Lett.*, 2011, **4**, 202–206.
6 E. P. Roth and C. J. Orendorff, *Electrochem. Soc. Interface*, 2012, **21**, 45–49.
7 C. Xu, B. Li, H. Du and F. Kang, *Angew. Chem., Int. Ed.*, 2012, **51**, 933–935.
8 F. R. McLarnon and E. J. Cairns, *J. Electrochem. Soc.*, 1991, **138**, 645–656.
9 S. Arouete, K. F. Blurton and H. G. Oswin, *J. Electrochem. Soc.*, 1969, **116**, 166–169.
10 B. Lee, H. R. Lee, H. Kim, K. Y. Chung, B. W. Cho and S. H. Oh, *Chem. Commun.*, 2015, **51**, 9265–9268.
11 J. Lee, J. B. Ju, W. I. Cho and S. H. Oh, *Electrochim. Acta*, 2013, **112**, 138–143.
12 C. Xu, H. Du, B. Li, B. F. Kang and Y. Zeng, *Electrochem. Solid-State Lett.*, 2009, **12**, A61–A65.
13 M. H. Alfaruqi, V. Mathew, J. Gim, S. Kim, J. Song, J. P. Baboo, S. H. Choi and J. Kim, *Chem. Mater.*, 2015, **27**, 3609–3620.
14 B. Lee, C. S. Yoon, H. R. Lee, K. Y. Chung, B. W. Cho and S. H. Oh, *Sci. Rep.*, 2015, **4**, 1–8.
15 D. Kundu, B. D. Adams, V. Duffort, S. H. Vajargah and L. F. Nazar, *Nat. Energy*, 2016, **1**, 16119.
16 M. H. Alfaruqi, V. Mathew, J. Song, S. Kim and J. Kim, *et al.*, *Chem. Mater.*, 2017, **29**, 1684–1694.
17 Z. Jia, B. Wang and Y. Wang, *Mater. Chem. Phys.*, 2015, **149–150**, 601–606.
18 L. Sharma and A. Manthiram, *J. Mater. Chem. A*, 2022, **10**, 6376–6396.
19 H. Pan, Y. Shao, P. Yan, Y. Cheng, K. S. Han, Z. Nie, C. Wang, J. Yang, X. Li, P. Bhattacharya, K. T. Mueller and J. Liu, *Nat. Energy*, 2016, **1**, 16039.
20 W. Sun, F. Wang, S. Hou, C. Yang, X. Fan, Z. Ma, T. Gao and C. Wang, *et al.*, *J. Am. Chem. Soc.*, 2017, **139**, 9775–9778.
21 C. W. Mason and F. Lange, *ECS Electrochem. Lett.*, 2015, **4**, A79–A82.
22 G. Li, Z. Yang, Y. Jiang, C. Jin, W. Huang, X. Ding and Y. Huang, *Nano Energy*, 2016, **25**, 211–217.
23 W. Li, K. Wang, S. Cheng and K. Jiang, *Energy Storage Mater.*, 2018, **15**, 14–21.
24 M. J. Park and A. Manthiram, *ACS Appl. Energy Mater.*, 2020, **3**, 5015–5023.
25 F. Wang, E. Hu, W. Sun, T. Gao, X. Ji, X. Fan, X.-Q. Yang, K. Xu and C. Wang, *Energy Environ. Sci.*, 2018, **11**, 3168–3175.
26 Q. Ni, H. Jiang, S. Sandstrom, Y. Bai, H. Ren, X. Wu, Q. Guo, D. Yu and X. Ji, *et al.*, *Adv. Funct. Mater.*, 2020, **30**, 2003511.
27 J. Rodríguez-Carvajal, *Phys. B*, 1993, **192**, 55–69.
28 P. Oberholzer, E. Tervoort, A. Bouzid, A. Pasquarello and D. Kundu, *ACS Appl. Mater. Interfaces*, 2019, **11**, 674–682.
29 Z. Xing, G. Xu, J. Han, G. Chen, B. Lu, S. Liang and J. Zhou, *Trends Chem.*, 2023, **5**, 380–392.
30 D. Bin and Y. Xia, *et al.*, *Adv. Funct. Mater.*, 2023, **33**, 2211765.
31 K. Momma and F. Izumi, *J. Appl. Crystallogr.*, 2011, **44**, 1272–1276.